Green upconversion emission dependence on size and surface residual contaminants in nanocrystalline ZrO 2 :Er 3+

Article *in* Journal of Sol-Gel Science and Technology · September 2012

DOI: 10.1007/s10971-012-2809-4

CITATIONS
3

READS
35

5 authors, including:

Luis Armando Diaz-Torres
Centro de Investigaciones en Optica
110 PUBLICATIONS **1,334** CITATIONS
SEE PROFILE

Pedro Salas
Universidad Nacional Autónoma de México
141 PUBLICATIONS **1,978** CITATIONS
SEE PROFILE

Octavio Meza Espinoza
Benemérita Universidad Autónoma de Puebla
24 PUBLICATIONS **205** CITATIONS
SEE PROFILE

Tzarara López-Luke
Centro de Investigaciones en Optica
47 PUBLICATIONS **231** CITATIONS
SEE PROFILE

Green upconversion emission dependence on size and surface residual contaminants in nanocrystalline $ZrO_2:Er^{3+}$

L. A. Diaz-Torres, P. Salas, C. Angeles-Chavez, O. Meza & T. Lopez-Luke

Journal of Sol-Gel Science and Technology

ISSN 0928-0707

J Sol-Gel Sci Technol
DOI 10.1007/s10971-012-2809-4

Springer

J Sol-Gel Sci Technol
DOI 10.1007/s10971-012-2809-4

ORIGINAL PAPER

Green upconversion emission dependence on size and surface residual contaminants in nanocrystalline $ZrO_2:Er^{3+}$

L. A. Diaz-Torres · P. Salas · C. Angeles-Chavez · O. Meza · T. Lopez-Luke

Received: 24 January 2012 / Accepted: 22 May 2012

Abstract The luminescence lifetime of the green upconversion emission Er^{3+} ions in ZrO_2 nanocrystals was found to be sensitive to the particle size and crystalline phase, as well as to the residual surface contaminants. Erbium doped (0.2 mol% Er_2O_3) ZrO_2 nanocrystals ranging from 54 to 120 nm in size were prepared by a sol–gel process with the presence of nonionic PLURONIC P127 surfactant, and the upconversion emission was characterized. PLURONIC P127 at a molar ratio of 0.0082 promoted both an enhancement in the green upconversion emission as well as a strong reduction of surface contaminants such as CO, CH_2, and OH. A fluorescence decay analysis via a simple microscopic rate equation model suggests that crystallite size and nonradiative relaxation mechanisms to different surface contaminants have to be taken into account to explain the observed green luminescence quenching. XRD, FTIR and luminescence lifetime measurements allow the quantification of the nonradiative processes that lead to the green luminescence quenching; and prove the relevance of using nonionic surfactants in the synthesis to reduce residual surface contaminants.

Keywords Upconversion · Erbium · Zirconium dioxide · Nanocrystals

L. A. Diaz-Torres (✉) · T. Lopez-Luke
Grupo de Espectroscopia de Materiales Avanzados y Nanoestructurados (EMANA), Centro de Investigaciones en Optica A. C., 37150 León, Guanajuato, Mexico
e-mail: ditlacio@cio.mx

P. Salas
Centro de Física Aplicada y Tecnología Avanzada, Universidad Nacional Autónoma de México, A.P. 1-1010, 76000 Santiago de Querétaro, Querétaro, Mexico

C. Angeles-Chavez
Instituto Mexicano del Petróleo, 07730 Mexico City, DF, Mexico

O. Meza
Instituto de Física, Universidad Autónoma de San Luis Potosí, Arturo Ortega #9, 78000 San Luis Potosí, Mexico

1 Introduction

Nanocrystalline materials have been recognized as having tremendous potential in the field of luminescence and thus are on the brink of revolutionizing the display and imaging industry [1, 2]. Many commercially available technological devices employ inorganic polycrystalline materials doped with lanthanide or transition metal ions as their main emissive component [3]. Once preparation methods were available to synthesize these phosphors in the nanometer regime, researchers compared the properties of these new luminescent materials versus already established commercially available materials and produced some very positive findings. The dependence of the luminescence intensity on the crystalline phase and size of the particle may be the result of changes in the (1) photon emission probability and—or (2) phonon emission probability [4]. To determine unambiguously which mechanism (1) or (2), dominates the luminescence intensity dependence on the crystalline phase and size of Er^{+3} doped ZrO_2 nanoparticles, we decided to investigate the luminescence dynamics of the $^4S_{3/2} \rightarrow {}^4I_{15/2}$ Er^{3+} transition. One of the most important parameters in the luminescence dynamic is the lifetime, and it can be written as $\tau = 1/(W_{RAD} + W_{NR} + W_{ET})$, where W_{RAD} is the radiative relaxation rate (photon emission) and W_{NR} is the nonradiative multiphonon relaxation (lattice phonon excitations). The term W_{ET} is the nonradiative energy transfer rate between neighboring rare earth ions, and for a dipole–dipole

Published online: 31 May 2012

interaction it scales with the inverse of the sixth power of the interatomic distance between the donor and the acceptor [5, 6]. We assume here that the contribution due to W_{ET} between Er ions is negligible because our samples have a very low concentration of Er^{+3} ions [7]. Hence, we are left with the two terms W_{RAD} and W_{NR}. The W_{RAD} term depends basically on the host lattice and symmetry sites where the Er^{3+} ions are substituted [8], while the W_{NR} term depends basically on the host phonon spectrum. Therefore, the lifetime may change as a result of modifications in the local symmetry, or the phonon spectrum, or both. The Er^{3+} green emitting level ($^4S_{3/2}$) has an energy gap to its closest lower lying excited state ($^4F_{9/2}$) around 2,900 cm^{-1} and the phonon energy of the ZrO_2 is 470 cm^{-1} [9]. Therefore a nonradiative relaxation downward ($^4F_{9/2}$) requires about 6 phonons, so the contribution of W_{NR} to the reduction of τ is negligible. If the W_{ET} between Er ions and W_{NR} are negligible, the changes in the lifetime of the green emitting level ($^4S_{3/2}$) need to be due to additional channels like nonradiative energy transfer processes from Er^{3+} ions to surface contaminants such as CH_2, OH^- or/and CO_2. The main vibration modes of CO_2, CH_2 and OH are around 2,350, 3,000 and 3,740 cm^{-1}, respectively. The CO_2 and CH_2 are more resonant that OH with the $^4S_{3/2} \rightarrow {}^4F_{9/2}$ nonradiative relaxation. In addition, the energy difference between CO_2 and CH_2 vibration modes is around one lattice phonon, whereas the OH vibration mode is almost two lattice phonons above the $^4S_{3/2} \rightarrow {}^4F_{9/2}$ nonradiative relaxation. Therefore, lattice phonon assisted nonradiative transitions from Er^{3+} to CO_2 and/or CH_2 are more probable than to OH.

In this work an estimation of the non radiative energy transfer rate (W_{ET}) from Er^{3+} to CO_2 and CH_2 are computed and discussed by means of a simple microscopic rate equation model. For these calculations the Er^{3+} ions considered to be inside of the nanocrystals whereas the residual contaminants are on the surface. Also, the nanocrystals phase and size are considered to compute the active ion distribution within the nanocrystals. Our model succeeds to fit the experimental emission fluorescence lifetime decays for the green upconversion emission from the $^4S_{3/2} \rightarrow {}^4F_{9/2}$ Er^{3+} transition; and the corresponding interaction parameters are reported.

2 Experimental

2.1 Sample preparation

ZrO_2 nanocrystals doped with 0.2 mol% of Er_2O_3 were prepared utilizing the sol gel method reported in previous works [10–14]. All chemicals used were of reactant grade, supplied by Aldrich, Inc. Nanoparticles of ZrO_2:Er^{3+} were obtained by mixing zirconium *n*-propoxide and erbium nitrate pentahydrate with a molar composition of 0.2 mol% Er_2O_3 with respect to ZrO_2. Care was taken in the addition of Er^{3+} to guarantee the same concentration in all prepared samples. In a typical preparation, 0.043 g of erbium nitrate was dissolved in 57 mL of ethanol and 10.9 mL of zirconium *n*-propoxide. After complete dissolution, 1.5 mL of nitric acid, 0.6 mL of hydrochloric acid, and 1.7 mL of distilled water were added. The surfactant, PLURONIC P127, was added 10 min later under strong stirring conditions. Surfactant was added at molar ratios Mrp = PLURONIC/ZrO_2 = 0 and 0.0082. The mixed solution was stirred for 1 h, and the resulting suspension was transferred into sealed Teflon autoclave. Hydrothermal treatment was carried at 80 °C for 24 h. After that, the autoclave was allowed to cool naturally and the gel was washed twice with absolute ethanol. Two samples (with Mrp = 0 and 0.0082) were annealed at to 1,000 °C, the heating rate was 5 1C/min and stayed at 300 and 500 1C for 2 h. Some samples were removed from the furnace as soon as the 1,000 °C were reached; we will denote this samples as annealing time 0 min. A third sample with an Mrp = 0.0082 was kept under the annealing process at 1,000 °C for 5 h. In all cases annealing was performed in ordinary air atmosphere.

2.2 Structural and morphology characterization

The X-ray diffraction (XRD) patterns were obtained using SIEMENS D5005 equipment provided with a Cu tube with Kα radiation at 1.5405 Å, scanning in the 20°–100° 2θ range with increments of 0.02° and a sweep time of 8 s. Transmission electron microscopy (TEM) was performed in JEM-2200FS transmission electron microscope with accelerating voltage of 200 kV. The Fourier transform infrared (FTIR) spectra were obtained using a Spectrophotometer Spectrum BX, FTIR system from Perkin-Elmer with a DTGS detector at 4 cm^{-1} spectral resolution and Beer-Norton anodization. Measurements were performed in the attenuated total reflectance (ATR) mode using 100 mg of ZrO_2:Er^{3+} powder covering the whole active area of the ATR device. The spectrum was obtained in the medium-infrared region from 1,000 to 4,000 cm^{-1} with 20 scans per spectra. Before measurements, the equipment was calibrated by verifying that the power energy was $\approx$80 % and the spectral response was calibrated with a polystyrene film as a reference.

2.3 Photoluminescence characterization

For the photoluminescence (PL) characterization a CW semiconductor laser diode centered at 970 nm was used as a pump source. The emission was analyzed with an Acton Spectra Pro 500i monochromator and a R955 Hamamatsu photomultiplier. The system was controlled with a PC where emission spectra were obtained. Lifetime curves

were measured using a chopper with a monochromator and photomultiplier connected to a LeCroy digital Oscilloscope. Samples were supported in 1 mm capillary tubes and measurements were done at room temperature. Special care was taken to maintain the alignment of the set up in order to compare the intensity of the upconverted signal between different characterized samples.

3 Results and discussions

3.1 Experimental results

The crystalline phase of $ZrO_2:Er^{3+}$ nanophosphor depends on the surfactant ratio and annealed time as can be seen in the XRD patterns in Fig. 1. For all samples, we find two phases: monoclinic and tetragonal, being the monoclinic phase the dominant one. All peaks in the XRD patterns in Fig. 1 were indexed either with JCPDS-37-1484 or JCPDS-50-1089 crystallographic standars, for the tetragonal and monoclinic structures, respectively. The monoclinic phases are 90, 78.8 and 95.1 wt% for samples (a) Mrp = 0 at 1,000 °C for 5 h, (b) Mrp = 0.0082 at 1,000 °C for 0 min and, (c) Mrp = 0.0082 at 1,000 °C for 5 h, respectively. The phase composition was estimated using the expression [15]:

$$C_m = \frac{I_m(\bar{1}11) + I_m(111)}{I_m(\bar{1}11) + I_m(111) + I_t(101)} \qquad (1)$$
$$C_t = 1 - C_m$$

where m and t stand for the monoclinic and tetragonal phase of the host and I stands for the integrated intensity of each peak. The crystallite sizes were estimated by the Scherrer's equation; see Table 1. Average crystallite sizes were 82 nm and 54 nm for samples with surfactant and annealed for 5 h and 0 min, respectively; whereas the sample without surfactant (annealed for 5 h at 1,000 °C) had an estimated crystallite size of 120 nm. Such crystallite sizes are in good agreement with the observed sizes in the TEM micrographs shown in Fig. 2.

Under NIR excitation at 970 nm, all nanocrystalline $ZrO_2:Er^{3+}$(0.2 %) samples presented a strong visible green emission, centered at approximately 550 nm and attributed to the $^4S_{3/2} \rightarrow {}^4I_{15/2}$ transition, see Fig. 3. No other visible Er^{3+} emission band was observed. It is clear from the green emission spectra in Fig. 3 that emission intensity increases first with surfactant addition and secondly with annealing time. That suggests that the intensity change is due to surface contaminants reduction promoted first by the presence of the surfactant, and secondly by the annealing process. It is worth to notice the increase of at least one order of magnitude in emission intensity due to the addition of surfactant and after 5 h of annealing time.

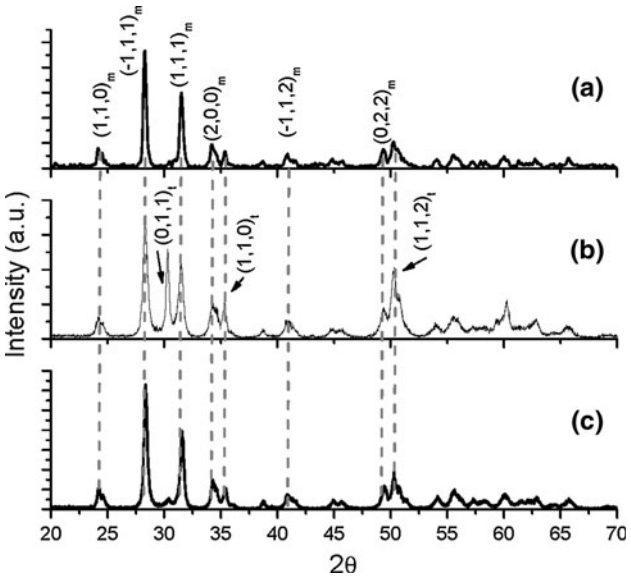

Fig. 1 XRD of $ZrO_2:Er^{3+}$(0.2 %) nanocrystals: **a** Mrp = 0 at 1,000 °C for 5, h **b** Mrp = 0.0082 at 1,000 °C for 0 min, and **c** Mrp = 0.0082 at 1,000 °C for 5 h. XRD peaks correspond to either tetragonal ("*t*" symbols) or monoclinic (*stars symbols*) structures, in agreement with JCPDS-37-1484 and JCPDS-50-1089 cards, respectively

Table 1 Parameters of the analysis of generalized pattern searches

Nanocrystal Size (nm)	54	82	120
Mrp	0.0082	0.0082	0
Annealing Time (h)	0	5	5
CO_2			
C_{06}^{CO} (cm^6s^{-1})	9.15×10^{-34}	9.15×10^{-34}	9.15×10^{-34}
R_{06}^{CO} (nm)	9.46	9.46	9.46
Surface density (ions/cm^2)	9.71×10^{13}	8.76×10^{13}	1.06×10^{15}
CH_2			
C_{06}^{CH} (cm^6s^{-1})	6.04×10^{-33}	6.04×10^{-33}	6.04×10^{-33}
R_{06}^{CH} (nm)	12.95	12.95	12.95
Surface density (ions/cm^2)	6.55×10^{10}	2.84×10^{10}	5.75×10^{14}

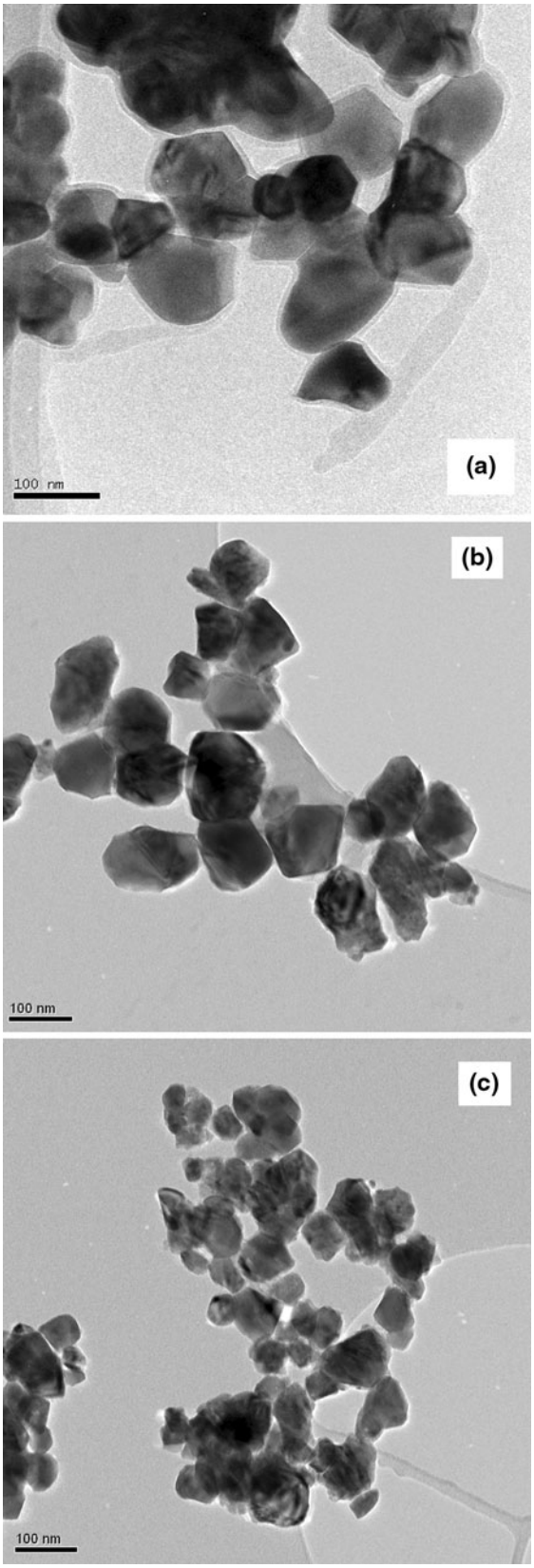

Fig. 2 TEM micrographs for nanocrystalline ZrO_2:Er^{3+}(0.2 %) samples: **a** Mrp = 0 at 1,000 °C for 5 h, **b** Mrp = 0.0082 at 1,000 °C for 5 h, and **c** Mrp = 0.0082 at 1,000 °C for 0 min

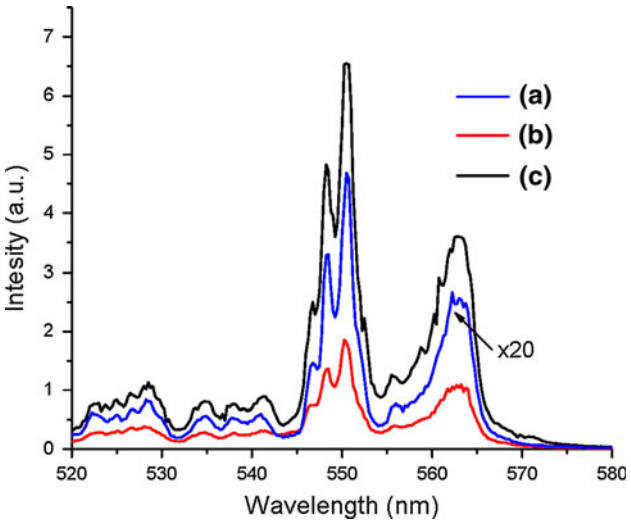

Fig. 3 Upconversion emission under 970 nm excitation of nanocrystalline ZrO_2:Er^{3+}(0.2 %) samples: (*a*) Mrp = 0 at 1,000 °C for 5 h, (*b*) Mrp = 0.0082 at 1,000 °C for 0 min, and (*c*) Mrp = 0.0082 at 1,000 °C for 5 h. *curve* (*a*) has been multiplied by 20 in order to be seen in the *graph*

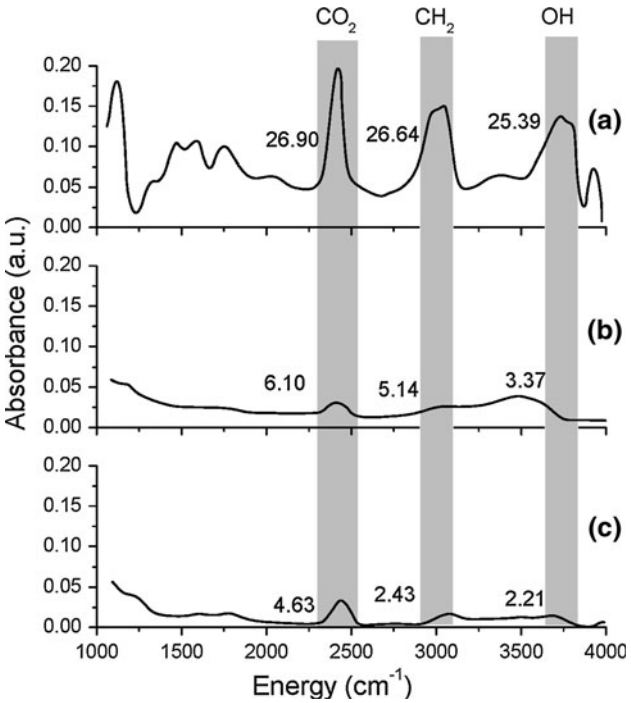

Fig. 4 FTIR spectra. of nanocrystalline ZrO_2:Er^{3+}(0.2 %) samples: **a** Mrp = 0 at 1,000 °C for 5 h, **b** Mrp = 0.0082 at 1,000 °C for 0 min, and **c** Mrp = 0.0082 at 1,000 °C for 5 h

The presence of organic residuals in the prepared samples was corroborated by performing FTIR spectroscopy and the spectra are shown in Fig. 4. The sample without surfactant (Fig. 4a) annealed for 5 h at 1,000 °C presents several resonant stretching bands associated with different residual components, 3,600–3,800 cm^{-1} (OH), 3,000 cm^{-1}

(CH_2), 1,500–1,750 cm^{-1} (CH–CH_2, OH), and 1,050 cm^{-1} (CH), and a resonant bending band at 1,200–1,400 cm^{-1} for (OH). The band centered at 2,350 cm^{-1} is associated with surface adsorbed CO_2, partly during the synthesis and partly from the environment during the measurement process, probably due to the granular characteristic of the nano powder. The absorbance spectrum integral for the bands associated to CO_2, CH_2 and OH in the ranges 2,288–2,578, 2,900–3,115 and 3,606–3,830 cm^{-1}, respectively, are depicted besides the bands (gray bands) in Fig. 4. The sample without surfactant has more CO_2 centers than the sample with surfactant and the subsequent annealing process reduces furthermore the CO_2 centers. The introduction of surfactant reduces the residual component, as can be observed in the FTIR spectrum displayed in Fig. 4 and was reported recently [10–14, 16, 17]. The surfactant works as a dispersing agent and its function is to weaken the organic bond.

The absorption peaks in curve a), of Fig. 5, correspond to transitions from the Er^{3+} ground state to the excited states at 15,300 cm^{-1} ($^4F_{9/2}$), 18,280 cm^{-1} ($^4S_{3/2}$) and 19,230 cm^{-1} ($^2H_{11/2}$). The corresponding first derivative of this absorption spectrum is depicted by curve b in Fig. 5. It is observed that the smaller difference between the $^4F_{9/2}$ and $^4S_{3/2}$ states is equal to 2,810 cm^{-1}. This energy is proportional to the energy gap between the $^4F_{9/2}$ and $^4S_{3/2}$ states and it is almost resonant to the bands centered at 2,350, 3,000 and 3,740 cm^{-1} associated with CO_2, CH_2 and OH, respectively. The experimental green upconversion emission fluorescence decays under 970 nm excitation changes with annealing time, see Fig. 6. The effective lifetime increases first with surfactant addition and

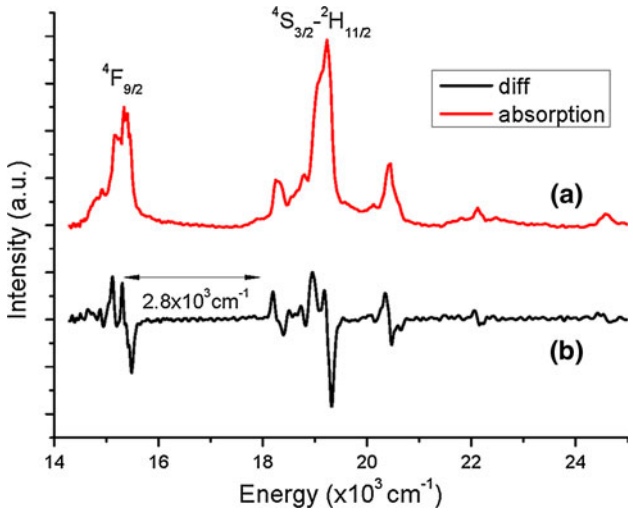

Fig. 5 The absorption spectra of the ZrO_2:Er^{3+} nanocrystals with Mrp = 0.0008 shown in *a*. In the *b* the derivative absorption spectra are reported. The lower difference between $^4F_{9/2}$ and $^4S_{3/2}$ is equal to 2,810 cm^{-1}

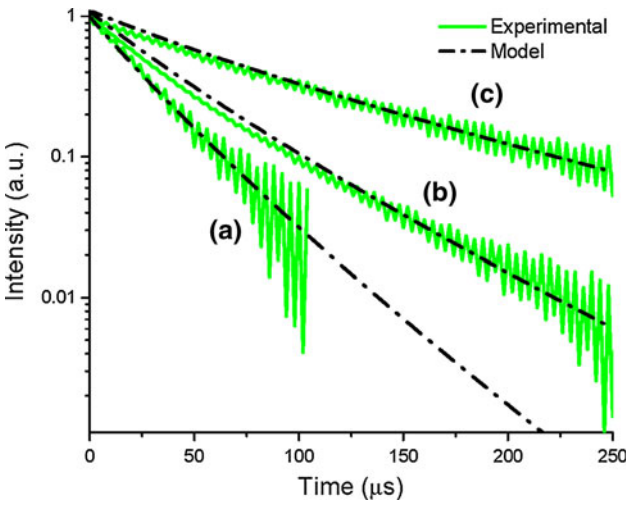

Fig. 6 *a* Simulations and experimental lifetime curves (*a*) Mrp = 0 at1000 °C for 5 h, (*b*) Mrp = 0.0082, at 1,000 °C for 0 min and (*c*) Mrp = at 0.0082, 1,000 °C for 5 h

secondly with the annealing time. Since the Er^{3+} concentration is the same for all samples and is quite small the non radiative energy transfer processes are negligible. Thus the observed increase in effective life time could be a result of surface contaminants reduction rather than non radiative energy transfer processes among Er^{3+} ions. Thus, the observed lifetime quenching can be attributed to non radiative energy transfers from the Er^{3+} ions to the residual surface contaminants.

3.2 Theoretical model

Up to now a wide variety of upconversion mechanisms have been reported. The majority of these involves some combination of absorption and nonradiative energy-transfer (ET) steps, see Fig. 7. Absorption may come in two basic

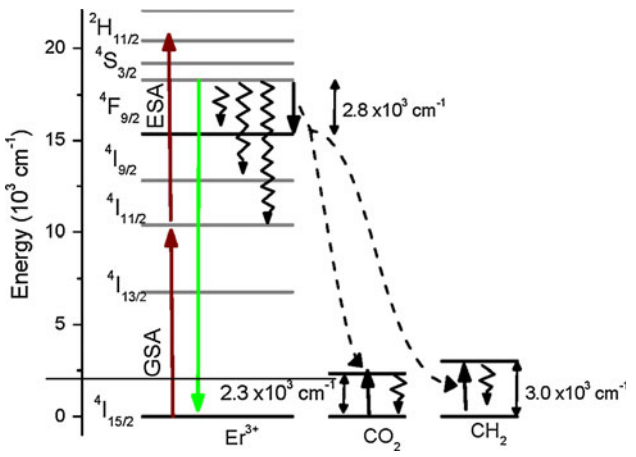

Fig. 7 Energy levels diagram of ZrO_2:Er^{3+}, direct Er^{3+} to CO_2 and CH_2 nonradiative energy transfer processes are considered as additional depopulation channels of the $^4S_{3/2}$ Er^{3+} level

forms. Ground state absorption (GSA, Fig. 7) that results from the promotion of Er^{3+} ion from its ground state to an excited state ($^4I_{15/2} \rightarrow {}^4I_{11/2}$); or Excited-state absorption (ESA, Fig. 7) that involves absorption of a photon by an excited ion, and results in promotion of that ion to a higher excited state ($^4I_{11/2} \rightarrow {}^4S_{3/2}$). The energy-transfer upconversion (ETU) is also possible, in which a Er^{3+} in $^4I_{11/2}$ energy level donates its excitation energy to a neighboring excited Er^{3+} in the same energy level, which is then promoted to a higher excited state ($^4S_{3/2}$). The dependence of ETU on concentration results directly from the strong dependence of the ET rate constant on the interionic distance [17–20], R, between the involved Er^{3+} ions. In this way, ET processes are very concentration dependent. At low dopant concentration levels in homogeneously doped crystals, where R is large, nonradiative energy transfer between Er^{3+} ions will be negligible leaving GSA + ESA as the only viable upconversion mechanism.

In order to study the intensity and lifetime quenching of the green emission we consider the possible relaxation processes that might take place once the Er^{3+} ions have reached its excited state ($^4S_{3/2}$), via the GSA + ESA process, see Fig. 7. Once the Er^{3+} ion is excited it can lose its energy either by radiative emission (green photon emission) or nonradiative energy transfer to the surface residual contaminants X (X=CO_2 or CH_2). Now, if $P_i\left(^4S_{3/2},t\right)$ is the probability to finding the *i*th Er^{3+} ion at its exited state ($^4S_{3/2}$) at the time t, we can write down a system of coupled rate equations that govern the fluorescence dynamics for all the Er^{3+} ions within an arbitrary nanocrystal:

$$\frac{dP_i\left(^4S_{3/2},t\right)}{dt} = -\frac{1}{\tau}P_i\left(^4S_{3/2},t\right) - P_i\left(^4S_{3/2},t\right)\sum_{j=1}^{N_{CO}} W_{ij}^{CO} - P_i\left(^4S_{3/2},t\right)\sum_{j=1}^{N_{CH}} W_{ij}^{CH} \tag{2}$$

$$\frac{1}{\tau} = \sum_x \left[W^{RAD}\left(^4S_{3/2} \rightarrow x\right) + W^{NR}\left(^4S_{3/2} \rightarrow x\right)\right], \tag{3}$$

$$W_{ij}^{CO} = \frac{C_{06}^{CO}}{R_{Er_iCO_j}^6},\ W_{ij}^{CH} = \frac{C_{06}^{CH}}{R_{Er_iCH_j}^6} \tag{4}$$

$$C_{06}^{CO} = \left(R_{06}^{C0}\right)^6 W^{RAD}\left(^4S_{3/2} \rightarrow {}^4I_{9/2}\right),\ C_{06}^{CH} = \left(R_{06}^{CH}\right)^6 W^{RAD}\left(^4S_{3/2} \rightarrow {}^4I_{9/2}\right) \tag{5}$$

where $1/\tau$ is the sum of the radiative (W^{RAD}) and nonradiative (W^{NR}) relaxation rates [21], with X = $^4I_{9/2}$, $^4F_{9/2}$, $^4I_{11/2}$ and $^4I_{13/2}$. It is worth to notice that W^{NR} stands for all non radiative pathways that are not comprised in the electron–phonon interactions with adsorbed CO_2 and CH_2. Thus, W_{ij}^{CO} is the nonradiative energy transfer rate from the *i*th Er^{3+} ion to the *j*th CO_2 separated by a $R_{Er_iCO_j}$ distance. W_{ij}^{CH} is the nonradiative energy transfer rate from the *i*th Er^{3+} ion to the *j*th CH_2 separated by a $R_{Er_iCO_j}$. C_{06}^{CO} and C_{06}^{CH} are the dipole–dipole microinteraction strength parameters [22, 23], and R_{06}^{CO} and R_{06}^{CH} are the Förster distances for the non radiative energy transfers from Er^{3+} ions to the CO_2 and CH_2 contaminants, respectively. N_{CO} and N_{CH} are the number of residual contaminants on the nanocrystal surface. The solution to Eq. (2) is,

$$P_i\left(^4S_{3/2},t\right) = P_i\left(^4S_{3/2},0\right)\exp(-t/\tau)\exp\left(-W_{ij}t\right) \tag{6}$$

with

$$W_{ij} = \sum_{j=1}^{N_X} W_{ij}^{CO} + \sum_{j=1}^{N_Y} W_{ij}^{CH}. \tag{7}$$

The overall fluorescence from the nanocrystal is proportional to the average probability of the Er^{3+}ion that remain excited at time t [14],

$$P\left(^4S_{3/2},t\right) = \frac{1}{N_{Er}}\sum_{i=1}^{N_{Er}} P_i\left(^4S_{3/2},t\right) = P\left(^4S_{3/2},0\right)\exp(-t/\tau)\sum_{i=1}^{N_{Er}}\frac{\exp\left(-W_{ij}t\right)}{N_{Er}}. \tag{8}$$

So experimental fluorescence decays could be fitted by this average solution (Eq. 8). In order to reduce the fitting error a parametric squared error equation is defined,

$$f = \left(\tau_{exp}^{i} - \tau_{model}^{i}\right)^2/\tau_{exp}^{i} + \left(\tau_{exp}^{ii} - \tau_{model}^{ii}\right)^2/\tau_{exp}^{ii} + \left(\tau_{exp}^{iii} - \tau_{model}^{iii}\right)^2/\tau_{exp}^{iii} \tag{9}$$

where $\tau_{exp}^{i}, \tau_{exp}^{ii}$ and τ_{exp}^{iii} are the effective experimental lifetimes of each of the samples: (1) Mrp = 0 at 1,000 °C for 5 h, (2) Mrp = 0.0082 at 1,000 °C for 0 min, and (3) Mrp = 0.0082 at 1,000 °C for 5 h, respectively. And $\tau_{model}^{i}, \tau_{model}^{ii}$ and τ_{model}^{iii} are the corresponding theoretical lifetimes obtained by

$$\tau_{model} = \int P\left(^4S_{3/2},t\right)dt/P\left(^4S_{3/2},0\right). \tag{10}$$

Thus, the squared error function f only depends on the unknown parameters N_{CO}, N_{CH}, C_{06}^{CO} and C_{06}^{CH}. In order to fit the model with the experimental results, f has to be minimized varying the unknown parameters. Once these parameters are calculated we can estimate the Förster distances (R_{06}^{CO} and R_{06}^{CH}) using the Eq. 5 and the Surface density (Assuming a spherical morphology) is equal to $N_X/\left(\pi d^2\right)$ for X=CO and CH and d = 54, 82 and 120 nm. The minimal value of f was found using the genetic algorithm named Analysis of Generalized Pattern Searches [24, 25] and

the fitting parameters are reported in the Table 1. There is a good agreement between the experimental lifetime curves and its corresponding probability fitting curves as is shown in Fig. 6. The slight discrepancies between the model and experimental lifetime curves are mainly due to the possible existence of additional excitation and de-excitation channels like non radiative energy transfer between Er^{3+} ions or other contaminants that have not been taken into account. It is worth to notice that the same microinteraction parameters C_{06}^{CO} and C_{06}^{CH} were used for the three studied samples. That is, the microinteraction parameters are characteristic of the Er^{3+}–CO_2 (or Er^{3+}–CH_2) interacting pair, and do not depend on either the Er^{3+} or CO_2 (or CH_2) concentrations. In addition, the fitting surface concentrations N_{CO} and N_{CH} were proportional to its corresponding FTIR absorbance spectrum integrals. N_{CO} and N_{CH} in general increase as particle size increases, as expected, but its values are one order of magnitude smaller for the particles synthesized without pluronic P127. So, the number of surface contaminants is greatly reduced in the pluronic derived nanoparticles, and that leads to a reduced quenching effect on the observed luminescence, see Fig. 6. Therefore, the contaminant's surface concentration is an important factor to take into account when trying to reduce fluorescence quenching. This supports the importance of seeking surfactants that help reduce the overall surface contaminants. In particular, those for which its vibrational modes are in the range from 2,450 to 3,350 cm^{-1}. The particle size of course is also an important parameter, and its effect deal with the proportion of the active ions that remain close enough to the nanocrystal surface and are likely to lose its energy via nonradiative energy transfer to the surface contaminants. If we consider that the probability for an energy transfer between a single Er^{3+}–CO_2 pair at a fixed distance (R_{ErCO_2}) is given by [26]

$$E = \frac{(R_{06}^{CO})^6}{R_{ErCO_2}^6 + (R_{06}^{CO})^6}. \tag{11}$$

Then, for Er–CO_2 distances smaller than R_{06}^{CO} the probability for the transfer process to take place is above 50 %. In this case, luminescent quenching is more likely and Er^{3+} ions will be losing energy to the CO_2 center on the nanocrystal surface. On the other hand, if the Er–CO_2 distance is larger than R_{06}^{CO} the energy transfer is less likely and the main relaxation for the Er^{3+} ions will be through emission of green photons. Then, for each nanocrystal it is possible to consider a superficial shell, with a depth around $R_{06}^{CO} = 9.46$ nm, such that if an Er^{3+} ions is within the shell, its fluorescence is likely to be quenched by energy transfer to the CO_2 centers in the nanocrystal surface. In correspondence, the Er^{3+} ions located within the remaining inner core of the nanocrystal will have almost no quenching in fluorescence. Thus for a given surface contaminant, CO_2 for example, if it is considered that the Er^{3+} ions are homogeneously distributed within the nanocrystal, the proportion of Er^{3+} ions that will be subject to quenching is proportional to the shell to nanocrystal volume ratio,

$$\frac{V_{Shell}}{V_{nanocryst}} = \frac{(d/2)^3 - (d/2 - R_{06}^{CO})^3}{(d/2)^3} = \left[1 - \left(1 - 2\frac{R_{06}^{CO}}{d}\right)^3\right] \tag{12}$$

where d is the diameter of the nanocrystal and R_{06}^{CO} is characteristic dipole–dipole microinteraction distance for the pair Er–CO_2. Now, if it is considered that the overall quenching of fluorescence is proportional to the number of Er^{+3} ions subject to strong energy transfers to CO_2 centers ($R_{ErCO2} < R_{06}^{CO}$), then Eq. (12) gives a good idea of how strong the fluorescence quenching is depending on the nanocrystal size d. Thus, as nanocrystal size increases the fluorescence quenching due to nonradiative energy transfer to contaminant surface centers will decrease, being of around 72, 54, and 40 % for nanocrystals with average sizes of 54, 82, and 120 nm, respectively. Of course, for nanocrystals smaller than $2R_{06}^{CO} = 18.92$ nm all active Er^{3+} ions will be subject to very strong quenching, 100 % inclusive. This is in agreement with fluorescence decays a) and b) in Fig. 6, for the samples synthesized with pluronic, but it is not for fluorescence decay c) which corresponds to the higher nanocrystal size. This disagreement is explained by the fact that such sample has the highest concentration of surface impurities. Therefore, the overall fluorescence quenching depends on two main parameters: (1) the distance ratios ($2R_{06}^{CO}/d$) and ($2R_{06}^{CH}/d$) and (2) the effective surface contaminants concentrations N_{CO}, N_{CH}. The characteristic distances R_{06}^{CO} and R_{06}^{CH} are the dipole–dipole interaction parameters and depend only on the nature of the Er^{3+}–CO_2 and Er^{3+}–CH_2 pairs, regardless of concentrations or synthesis processes; whereas N_{CO}, N_{CH}, and d depend on the synthesis process and to a grand extend on the use or not of surfactants, and annealing processes. In resume, there is a compromise between size and surface contaminant concentration. As size increases overall quenching due to surface effects (shell for energy transfer interaction) decreases, but for larger nanocrystal size the surface contaminants will be greater (for example the sphere surface is $A(r) = 4\pi r^2$) and these contaminants reduce the luminescence.

4 Conclusions

In summary, we studied the upconversion green emission dynamics of ZrO_2:Er^{3+} as a function of nanocrystal's size

and surface residual contaminants concentrations. Estimation of W_{ET} between Er^{3+} and surface residual CO_2 and CH_2 are calculated and discussed by a microscopic rate equations model. Our model succeeds to fit the green upconversion curves lifetime and the corresponding interaction parameters are reported. The overall fluorescence quenching depends on two main parameters: (1) the distance ratios ($2R_{06}^{CO}/d/$) and ($2RR_{06}^{CH}/d$) and (2) the effective surface contaminants concentrations N_{CO}, N_{CH}. The characteristic distances R_{06}^{CO} and R_{06}^{CH} are the dipole–dipole interaction parameters and depend only on the nature of the Er^{3+}–CO_2 and Er^{3+}–CH_2 pairs, regardless of concentrations or synthesis processes; whereas N_{CO}, N_{CH}, and nanocrystallite size depend on the synthesis process, and to a grand extend on the use or not of surfactants and annealing processes. In resume, there is a compromise between size and surface contaminant concentration. As size increases overall quenching due to surface effects (shell for energy transfer interaction) decreases, whereas as size and in turn overall surface increases the surface′s contaminants concentration increases and in turn overall quenching increases.

References

1. Liu X, Dong G, Qiao Y, Qiu J (2008) Appl Opt 47(34): 6416–6421
2. Wang G, Peng G, Li P (2011) Acc Chem Res 44(5):322–332
3. Lüer L, Manzoni C, Egelhaaf HJ, Cerullo G, Oelkrug D, Lanzani G (2006) Physical Review B 73(3):035216
4. Ghosh P, Patra A (2005) Pramana – J Phys 65(5):901–907
5. Shaw PE, Ruseckas A, Samuel IDW (2008) Physical Review B 78(24):245201
6. Kim D, Okahara S, Nakayama M, Shim Y (2008) Physical Review B 78(15):153301
7. Gamelin DR, Gamelin DR (2001) Top Curr Chem 214:5–23
8. Zhu Q, Li J-G, Li X, Sun X (2009) Acta Mater 57(20):5975–5985
9. Chen G, Somesfalean G, Liu Y, Zhang Z, Sun Q, Wang F (2007) Physical Review B 75(19):195204
10. Lopez-Luke T, De la Rosa E, Salas P, Angeles-Chavez C, Diaz-Torres LA, Bribiesca S (2007) J Phys Chem C 111(45): 17110–17117
11. Angeles-Chavez C, Salas P, Lopez-Luke T, de la Rosa E (2010) Vacuum 84:1226–1231
12. Solis D, Lopez-Luke T, De la Rosa E, Salas P, Angeles-Chavez C (2009) J Lumin 129:449–455
13. Salas P, Nava N, Ángeles-Chavez C, De la Rosa E, Díaz-Torres LA (2008) J Nanosci Nanotechnol 8:6431–6436
14. Meza O, Diaz-Torres LA, Salas P, Rosa EDl, Angeles-Chavez C, Solis D (2009) Journal of Nano Research 5:121–134
15. Garvie RC, Nicholson PS, Am J (1972) Ceram Soc 55(6): 303–305
16. Hong SJ, Han JI (2007) J Electroceram 18:67–71
17. De G, Qin W, Zhang J, Zhang J, Wang Y, Cao C, Cui Y (2006) Solid State Commun 137(9):483–487
18. Nakamura T, Ogawa T, Adachi S, Fujii M (2009) Physical Review B 79(7):075309
19. de Sousa DF, Nunes LAO (2002) Physical Review B 66(2): 024207
20. Caldiño U, Jaque D, Martín-Rodríguez E, Ramírez MO, García Solé J, Speghini A, Bettinelli M (2008) Physical Review B 77(7): 075121
21. Gómez LA, Maciel GS, Araújo CBd, Patra A (2008) J Appl Phys 103(5):053507
22. Wolber PK, Hudson BS (1979) Biophys J 28(2):197–210
23. Rai S, Hazarika S (2008) Opt Mater 30(9):1343–1348
24. Lewis RM, Torczon V (2002) SIAM J Optim 12(4):1075–1089
25. Audet C, Dennis JJE (2002) SIAM J Optim 13(3):889–903
26. Lakowicz JR (2006) Principles of fluorescence spectroscopy, 3rd edn. Springer, Berlin, pp 13–14